THE JOURNAL OF PHYSICAL CHEMISTRY C

A JOURNAL OF THE AMERICAN CHEMICAL SOCIETY

December 14, 2023
Volume 127
Number 49
pubs.acs.org/JPCC

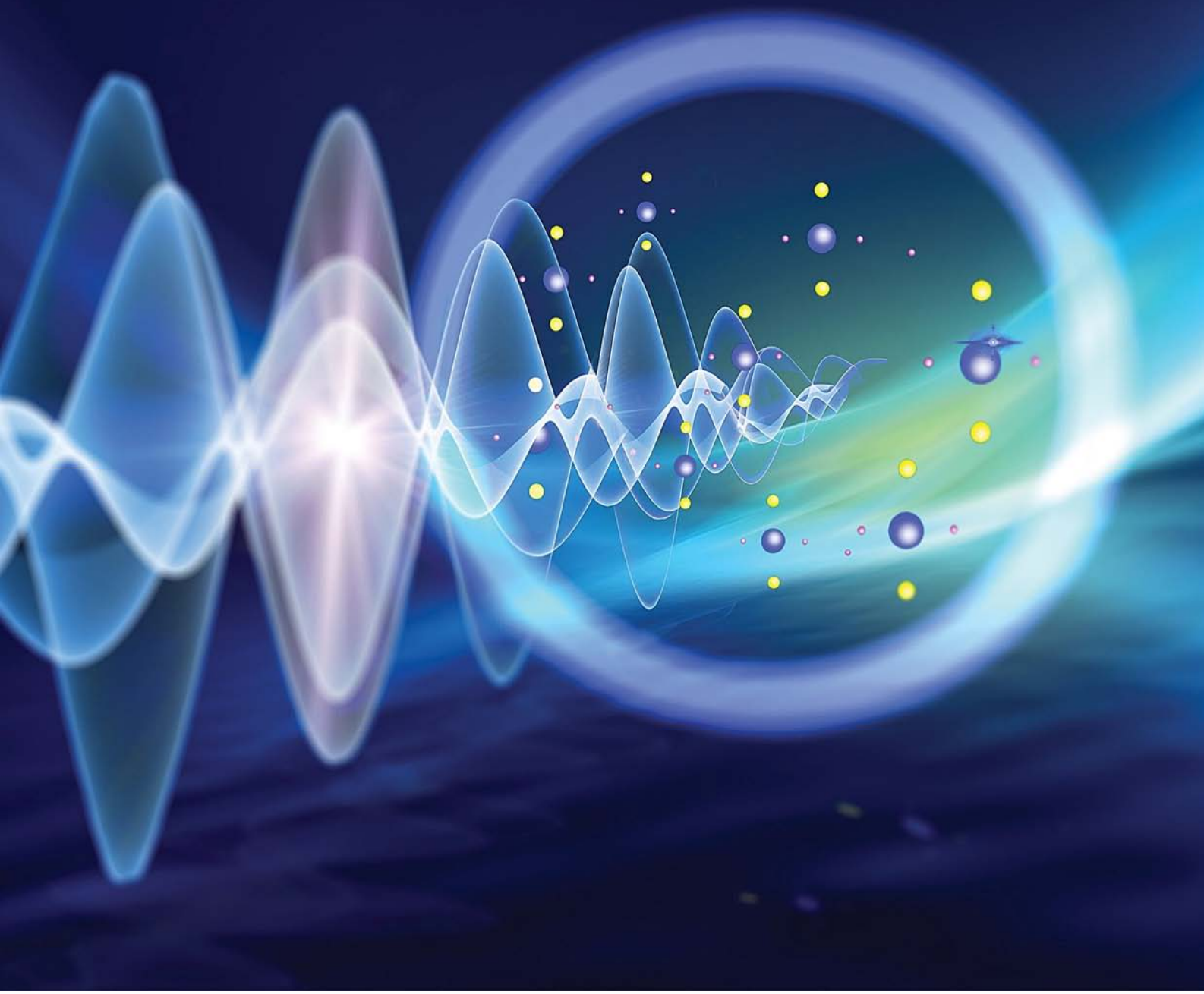

ACS Publications
Most Trusted. Most Cited. Most Read.

www.acs.org

THE JOURNAL OF PHYSICAL CHEMISTRY C
A JOURNAL OF THE AMERICAN CHEMICAL SOCIETY

pubs.acs.org/JPCC

Article

Improvement of Stability and Optoelectronic Properties of Blue-Emitting Perovskite Nanoplatelets by Microwave Treatment

Published as part of The Journal of Physical Chemistry C virtual special issue "The Physical Chemistry of Perovskites".

Ruxue Li,* Yuanxun Liu, Ziyuan Xie, Xuanyu Zhang, Huafeng Shi, and Rui Chen*

Cite This: *J. Phys. Chem. C* 2023, 127, 23917−23925

Read Online

ACCESS | Metrics & More | Article Recommendations

ABSTRACT: In this work, low-dimensional blue-emitting $CsPbBr_3$ nanoplatelets were prepared. Changes in the surface morphology of NPLs after long-term storage in a humid environment were observed by transmission electron microscopy. The reason for the $CsPbBr_3$ NPLs emission change from blue to green is found to be the loss of ligand and ion migration. Microwave treatment was demonstrated to improve the photostability and electrical stability of the samples. Based on the temperature-dependent and power-dependent photoluminescence measurement, it was concluded that both surface and internal defects of the sample decrease after microwave treatment. The ultrafast decay pathway of perovskite was thoroughly analyzed, and the ligand loss was found to be a deprotonation process, while the ion migration is a vacancy-driven and charge redistribution process. After microwave treatment, the residual polar DMSO solvent volatilizes, reducing the chance of structural collapse, and the surface and internal structural defects are reduced. In turn, the Br^- ion can exist more stably on its surface. As a result, the defect migration pathway is reduced, and photostability and smaller magnitude photocurrent hysteresis can be obtained, which will provide an effective strategy for the optimization and stability improvement of blue-light optoelectronic devices.

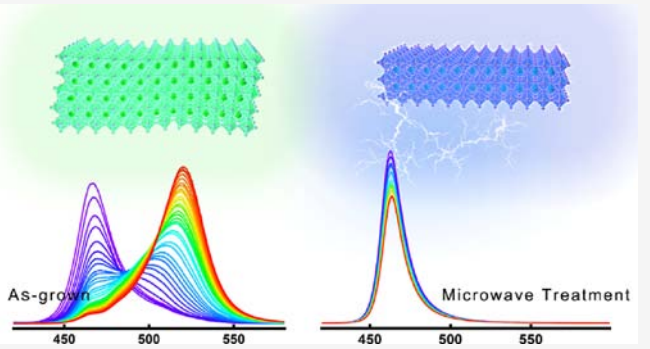

INTRODUCTION

In recent years, metal halide perovskite materials have attracted great scientific and technological interest due to their excellent photovoltaic and optoelectronic properties, such as a long carrier diffusion length, high mobility, flexible band-gap tuning, a high photoluminescence quantum yield (PLQY), and high defect tolerance.[1−5] Many advantages, including facile synthesis, solution processability, and low costs, make perovskites to be of great potential in photovoltaics and light-emitting devices (LEDs). Therefore, the perovskite-based LEDs (PeLEDs) have achieved considerable progress,[6−9] reaching external quantum efficiency (EQE) of more than 23% for green[10] and red[11] and more than 20% for near-infrared emissions.[12] Nevertheless, blue-emitting PeLEDs, an indispensable core component of solid-state lighting, have not yet reached an impressive level as that of green- and red-emitting devices. It is even more challenging to achieve high EQE and luminance in a pure blue color (emission below 475 nm) due to the poor performance inherited from pure chloride perovskites of which efficiencies are usually below 10%.[13−15] Previously, the blue-emitting perovskite has been obtained using polycrystalline films or nanocrystals (NCs) made from 3D or 3D/2D perovskites with mixed Cl−Br compositions.[16,17] However, halides will tend to separate into Cl- and Br-rich domains at a high applied bias or under light irradiation, lowering the EQE and causing an emission shift in the electroluminescence (EL) and photoluminescence (PL).[18,19] This phase separation stems from ion migration and particularly different activation energies (E_a) of the ion migration of Br and Cl (0.25 eV for $CsPbBr_3$ and 0.29 eV for $CsPbCl_3$),[20] which is proven to be the main reason of photocurrent hysteresis and will also accelerate the degradation of perovskite-based electronic devices. Unfortunately, there is no good solution so far to solve this problem, and thus, hybrid halide perovskites are not ideal materials for high-performance blue LEDs so far. Alternatively, utilizing strong quantum

Received: September 1, 2023
Revised: November 2, 2023
Accepted: November 2, 2023
Published: November 20, 2023

confinement of pure bromide-based perovskites is another promising way to obtain blue emission.[21,22] Nevertheless, it is still a challenge to synthesize stable NCs with particle sizes smaller than the exciton Bohr radii of $CsPbBr_3$ (7 nm). Proven and researched for a long time, colloidal perovskite nanoplatelets (NPLs) are the best strategy to break this dilemma, and researchers have achieved a fascinating PLQY of 96% for the ultrapure blue emission at 462 nm from $CsPbBr_3$ NPLs.[23] Although great progress has been made in the luminescence of blue emission of perovskites, some existing potential threats still need to be addressed. It has been reported that NPLs require more organic ligands for latitude confinement, while the action of oleic acid (OA) and oleylamine (OAm) via hydrogen bonding on the surface halide atoms of perovskite NCs is highly dynamic. Such a dynamic binding nature is suggested to be the origin of ligand loss and thus EQE deterioration.[24,25] Additionally, residual polar solvents such as DMF and DMSO can easily decompose PQDs and cause surface defects.[26,27] Furthermore, there are also halogen vacancy defects that accelerate ion migration pathways[28,29] as well as well-known environmental conditions such as with water, air, and light that will cause the instability of the perovskite.[30−32] In general, there are many factors affecting the emission efficiency of blue-emitting perovskites.

It has been reported that some strategies have been for improving stability, such as surface hydrophobic film-coating, addition of a natural hydrophobic structure, passivation, thermal annealing, and so on.[33−37] However, the surface coating will affect electrical injection, while the chemical method used in the passivation method is complicated and can easily cause unknown changes. The thermal annealing can easily lead to the structural collapse of perovskite. Among the numerous optimization methods, noncontact electromagnetic wave post-treatment, such as UV and microwave annealing, showed simple but excellent performance.[38−40] The improper use of UV light will bring irreparable damage to the perovskite owing to the shallow penetration depth. Meanwhile, for the microwave treatment, it has a long penetration depth, and most of the lattice defects, especially vacancy defects, can be suppressed instantaneously. In addition, it is worth noting that the polar solvent can instantly reach its boiling point under microwave treatment (the ability of the polar solvent to absorb microwaves is much greater than that of the perovskite); therefore, the residual polar solvent will be eliminated. Therefore, microwave treatment has been considered to be a better choice for improving low-dimensional perovskites. On the other hand, due to the limitation of characterizations, the interion reaction of perovskite is too fast to be observed, and thus, there are still different opinions on the origin of the decay pathway, the role of ligands, and the ion migration in perovskite. Although the full implications of this ion migration are currently elusive, many theoretical and experimental studies have shown that halide anions are the dominant mobile ions and are closely related to vacancy defects in the structure. Therefore, it is urgent to take a clear picture of the reasons for the emission efficiency attenuation of blue emission perovskite and to propose an effective improvement strategy based on this, which is of great significance for promoting the perovskite solid-state lighting industry.

In this work, low-dimensional blue-emitting $CsPbBr_3$ NPLs were fabricated. The changes of the surface topography of NPLs after a long time of being stored in moisture circumstances were observed by transmission electron microscopy (TEM). It was found that the reason the blue-emitting $CsPbBr_3$ turns green is the loss of ligands and the consequent ion migration. The as-grown samples were treated by microwave treatment under different conditions. From the results of temperature- and power-dependent PL, it was concluded that both surface and internal defects of the samples were suppressed after microwave treatment. The change of femtosecond carrier dynamics due to microwave treatment was observed by ultrafast absorption spectroscopy, and an in-depth analysis of the perovskite decay pathway will be shown. It was found that the cooling process of hot carriers plays an important role in this process. The loss of ligands is a process that is vacancy-driven and of deprotonation and charge redistribution. The blue-emitting $CsPbBr_3$ after microwave treatment shows good photostability and smaller magnitude photocurrent hysteresis, demonstrating that the reduction of the internal defect density is beneficial for reducing the degree of deprotonation of the ligands and ion migration.

EXPERIMENTAL SECTION

Synthesis of NPLs. Lead bromide ($PbBr_2$, 99.999%) was purchased from Aladdin. Oleylamine (OAm, 90%), 1-octadecene (ODE, 90%), and cesium carbonate (Cs_2CO_3, 99.9%) were obtained from Adamas-beta. Methyl acetate (98%), hexane (97.5%), and toluene (99%) were purchased from General Reagents. Oleic acid (OA, 90%) and isopropyl alcohol (IPA, 99.7%) were received from Alfa Aesar and Shanghai Lingfeng, respectively. Perovskite $CsPbBr_3$ NPLs were synthesized through a modified microemulsion method. One millimole of $PbBr_2$ was ultrasound-dissolved in 2 mL of DMSO to form a $PbBr_2$ precursor. One millimole of CsBr and moderate SA (0 or 2.3 mmol) were dissolved in 2 mL of hydrobromic (HBr) acid to form a CsBr precursor. All steps were carried out at room temperature. A volume of 0.5 mL of OAm and OA was added into 8 mL of toluene with 800 rpm stirring, respectively. Then, 100 μL of $PbBr_2$ precursors and CsBr precursors solution was dropped into the OA, OAm, and toluene mixed solution, respectively. After 6 s, 0.5 mL of butanol was added into the solution rapidly and stirred for 3 min later.

Characterization. TEM with an FEI Tecnai G2 F20 microscope operated at 200 kV was used to observe the size and shape of the $CsPbBr_3$ NPLs. UV−vis absorption spectra were recorded at room temperature on an ultraviolet and visible spectrophotometer. Steady-state PL spectra were measured by a Shamrock spectrometer (model no. SR-750-D1-R) and detected by a Newton CCD (model no. DU920P-BU). A He-Cd CW laser with a line of 325 nm as the excitation source was used to perform PL and long-time irradiation measurements. The power of the excitation laser was 1 mW, and the spot size was approximately 0.03 cm^2. For temperature-dependent PL measurements, the sample films were placed into a closed cycle helium cryostat (Cryo Industries of America) with quartz windows, and the temperature was controlled by a commercial temperature controller (Lakeshore 336) from 50 to 300 K. A He-Cd CW laser with a wavelength of 325 nm as the excitation source was used to perform temperature-dependent PL. The 355 nm femtosecond pulses were selected (Coherent Astrella ultrafast Ti:sapphire laser with OperA Solo, a pulse with 100 fs, and a repetition rate of 1000 Hz) to perform the power-dependent PL measurement and time-resolved PL decay curves.

https://doi.org/10.1021/acs.jpcc.3c05919
J. Phys. Chem. C 2023, 127, 23917−23925

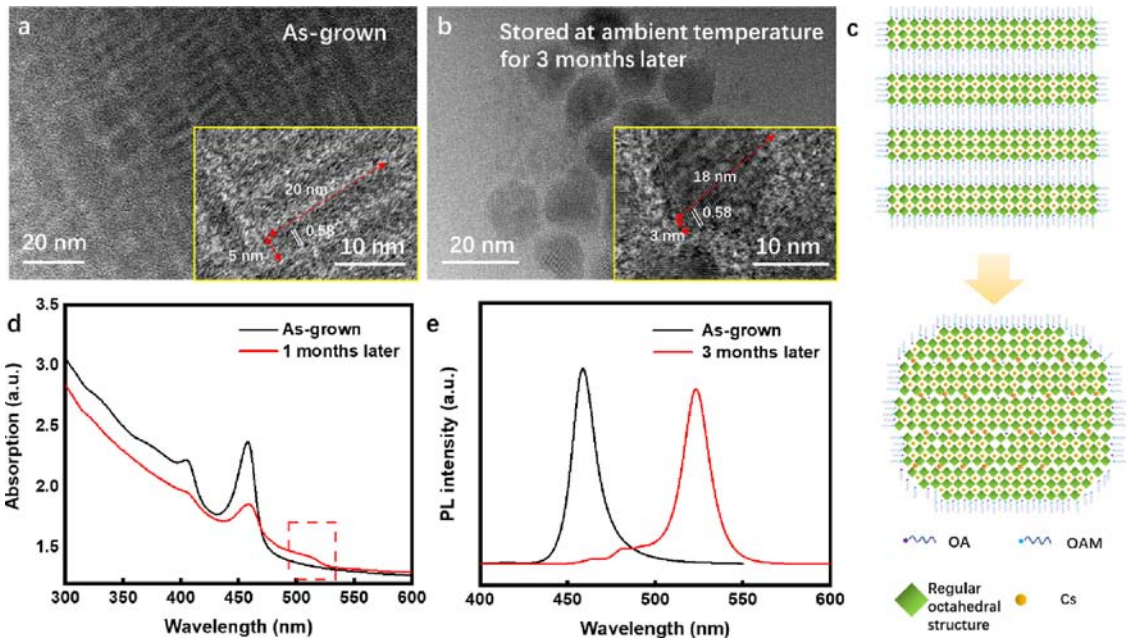

Figure 1. Characteristics of low-dimensional blue-emitting $CsPbBr_3$NPLs before and after a long time stored in at ambient temperature. (a, b) TEM images of the as-grown sample and the sample stored at the ambient temperature for three months. Insets are the corresponding magnified figures. (c) Schematic of lacking ligands and peripheral ions to aggregate into large-sized structures. (d) Absorption spectra of the as-grown sample and the sample stored at the ambient temperature for 1 month. (e) Room-temperature PL of the as-grown sample and the sample stored at ambient temperature for three months.

Microwave Treatment and Device Fabrication. Midea M1L-213C equipment was used for the microwave treatment. The selected power of the microwave radiation was 800 W for 3−30 s. The $CsPbBr_3$ NPLs were spin-coated onto a clean quartz substrate by deposition at 2000 rpm for 45 s. Then, silver electrodes (100 nm) were deposited in a thermal evaporation system.

RESULTS AND DISCUSSION

Figure 1a,b shows the TEM of the low-dimensional blue-emitting $CsPbBr_3$ NPLs before and after three months at the ambient temperature. It can be seen that the as-grown $CsPbBr_3$ NPLs have a rectangular shape with a length of approximately 20 nm and a width of 5 nm. In contrast, the samples stored at the ambient temperature for three months were visibly clustered, exhibiting a circular shape and a diameter of approximately 18 nm. The insets are the enlarged TEM image of the samples, and the circle-shape aggregation is formed by a number of rectangular aggregates. As demonstrated in Figure 1c, it can be clearly seen that the absence of ligands and peripheral ions between the rectangular NPLs will gradually compress and aggregate toward the center, eventually turning into round-like nanocrystal samples. The UV−vis absorption spectra of the sample stored at ambient temperature for 1 month show absorption at approximately 518 nm, whereas the absorption of a freshly grown sample was at 464 nm, as plotted in Figure 1d. When the sample was stored for three months, the emission from the sample turned completely green, as shown in Figure 1e. Therefore, it can be concluded that the main reason for the transformation of the low-dimensional blue-emitting perovskite into green is the absence of ligands and peripheral ions in the structure as well as the aggregation into larger sizes.

In order to improve the stability of low-dimensional blue-emitting perovskite, microwave treatment with different conditions were used. Figure 2a is the schematic diagram of the sample under microwave treatment for 3−30 s, and the samples were indexed as MW-3s to MW-30s, respectively. Figure 2b,c shows the enhancement of absorption and integrated PL intensity of the microwave-treated samples compared with the as-grown sample under different treated conditions. It can be seen in Figure 2b that the absorption reaches the maximum enhancement for the sample MW-10s. While the emission reaches its maximum for the sample MW-5s, the sample MW-10s decreases. It implies that MW-10s have a larger absorption value, but the ability to light conversion decreases, which indicates that the defects of MW-10s increase. Therefore, the microwave treatment of 5 s is considered to be the optimal condition. To prove this conjecture, temperature-dependent and power-dependent PL measurements were carried out, and the results are shown in Figure 2d,e, respectively. It can be seen from Figure 2d that both the as-grown and MW-5s show the decrease of the PL intensity for temperatures below 200 K, while the reverse trend is observed with temperatures above 200 K. It has been confirmed that the unusual PL quenching phenomenon is related to the surface states of the samples.[41] At low temperatures, surface defects will capture electrons, which results in nonradiative recombination. Above a certain critical temperature, electrons will escape from the defect states and participate in radiative recombination, which give rise to the enhanced emission. Thus, the emission enhancement reflects the magnitude of the defect density in the material, and a larger enhanced value indicates a higher density of surface defects. As shown in the figure, it can be seen that the PL enhancement of the as-grown sample is higher than that of the MW-5s sample, which implies that the density of surface defects is higher in the as-grown sample than in the MW-5s sample. In order to further analyze the suppression of defects after microwave treatment, the methodology of our previous work was used.[33] A low fluence

https://doi.org/10.1021/acs.jpcc.3c05919
J. Phys. Chem. C 2023, 127, 23917−23925

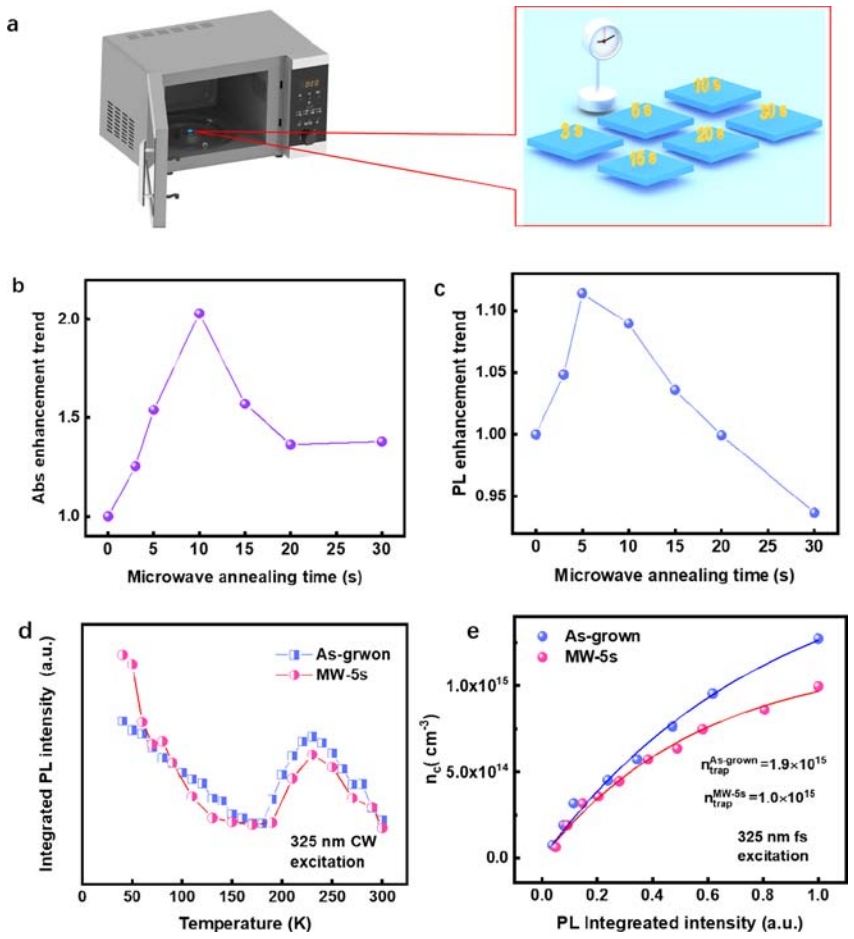

Figure 2. Evolution of the defect concentration of samples before and after microwave treatment. (a) Schematic diagram of microwave treatment. (b, c) Enhancement of the absorption and integrated PL intensity of the microwave-treated samples compared with the as-grown sample under different treated conditions. (d) Temperature-dependent PL intensity of the as-grown and MW-5s samples. (e) Evolution of the defect concentration of the as-grown and MW-5s samples as a function of photogenerated carrier density.

of femtosecond laser pulses at 325 nm (the penetration depth of this laser is larger than the thickness of the sample) was used for measurement due to the negligible trap states' depopulation during the luminescent period.[33] Ultrafast femtosecond pulses can prevent the trap-state depopulation during the excitation process, which enables a more accurate determination of the density of trap states. Figure 2e shows the variation of internal defect concentrations with the density of photogenerated carriers, and the defect concentration of the MW-5s sample are lower than the as-grown sample, which are $n_{trap}^{MW\text{-}5S} = 1.0 \times 10^{15}$ and $n_{trap}^{as\text{-}grown} = 1.9 \times 10^{15}$, respectively. This indicates that the internal defects of the sample are reduced after microwave treatment. Therefore, the microwave treatment can reduce the defect density on the surface and inside the perovskite at the same time.

To illustrate the carrier dynamics and hot carrier relaxation processes of the samples before and after microwave treatments, ultrafast transient absorption (TA) spectroscopy is used to measure the samples as shown in Figure 3. The corresponding light irradiation samples are named as as-grown-L and MW-5s-L, respectively. A pump pulse at 355 nm at 9.4 W/m^2 (with an initial carrier concentration: $N_0 = 9.4 \times 10^{17}$ cm^{-3}; ~100 fs and 1 kHz) was used to excite. The TA spectra and corresponding pseudocolor pictures of the as-grown and microwave-treated samples as well as the corresponding light-irradiated samples for 30 min are shown in Figure 3a,b. As shown in the figures, two negative photobleaching (PB1 and PB2) peaks at positions of 400 and 456 nm is shown in the as-grown sample, and another negative PB3 peak appears in the as-grown-L sample. The PB2 peak originates from the ground-state bleaching (GSB) because of the state filling of the carriers at the band edge. The PB1 peak originates from interstitial defects at high energy levels on the conduction band, and the PB3 peak originates from the bleaching signal at the energy level produced by the ion clusters after light irradiation.[42,43] Meanwhile, the MW-5s and the MW-5s-L samples only appear to have one negative PB peak at 456 nm. Therefore, the peak intensity of PB1 represents the number of interstitial defects (internal defects) in the as-grown sample. As can be seen from Figure 3a, PB1 disappeared in the microwave-treated sample, indicating the removal of interstitial defects in the samples after treatment. In addition, the PB3 peak comes from the newly appeared defects of the sample, which comes from ion stacking cluster on the surface after light irradiation.[44] It is noted that the PB3 does not exist in the sample after microwave under illumination, which indicates that the surface defects of the NWs-5s sample had been passivated, and there was no obvious ion stacking cluster after light irradiation in the MW-5s-L sample. This result is also confirmed in the corresponding pseudocolor pictures (Figure 3b). It shows that all samples were found to be blue-shifted and then red-shifted. The blue

https://doi.org/10.1021/acs.jpcc.3c05919
J. Phys. Chem. C 2023, 127, 23917−23925

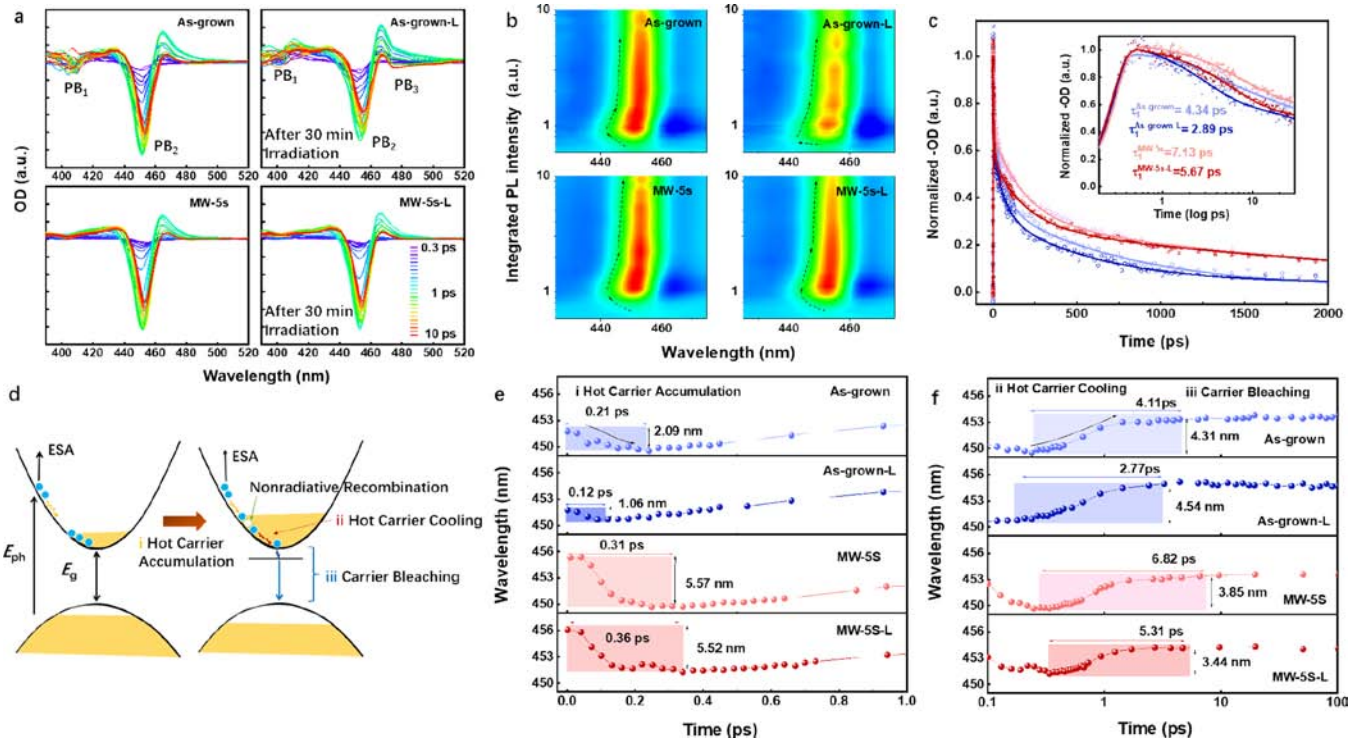

Figure 3. Influence of microwave treatment and light irradiation on carrier dynamics. (a, b) fs-TA spectra and corresponding pseudocolor pictures of the as-grown and microwave-treated sample as well as the corresponding light excited samples for 30 min. It was pumped by 355 nm at 9.4 W/m^2 (with an initial carrier concentration of $N_0 = 9.4 \times 10^{17}$ cm^{-3}), and the same power was used for light irradiation. The dotted line in b shows the trend of the GSB with time. (c) fs-transient kinetic traces of the respective GSB maxima (456 nm) of the corresponding samples. The hollow marks in the figure are measured data, and the solid lines are fitted curves. The inset is an enlarged section within 30 ps. (d) Schematic of the energy band structure and electron transition of the blue emission perovskite NPLs. (e) Extracting the peak position of the ground-state bleaching signal as a function of time in b.

shift of the samples after microwave treatment was bigger than that of the as-grown samples, and the red shift showed the opposite trend. The blue-shift is the accumulation of hot carriers, and the red shift is the many-body Coulombic interaction induced by the hot carrier cooling, which in turn leads to the reorganization of energy bands. According to the previous study,[42] the hot carriers' cooling dynamics is governed by the intrinsic properties of materials, and these processes can reflect the amount of carrier migration pathways in the material. Generally, the faster the hot carrier rates (the shorter the lifetime, as shown in Figure 3c), the more energy is transferred to the ion migration pathway and the more unstable the structure. Thus, it can be known that the bigger blue shift, the weaker the red shift and the less ion migration exists in the microwave-treated sample.

The decay kinetics of each GSB is extracted and shown in Figure 3c with their fitting parameters listed in Table 1. These processes can be depicted in the schematic of the energy band structure and electron transition of the blue-emitting perovskite NPLs, as shown in Figure 3d. The fast decay component τ_1 bleaching is ascribed to the carrier transfer from lower species (donor domain) to the emitting domain, showing the hot carrier accumulation and cooling process. The slow decay component τ_2 shall refer to the charge trapping according to previous reports,[39,42] and the longtime decay component τ_3 is ascribed to the radiation composite lifetime. It was found that the hot carrier lifetime, the trap lifetime, and the radiation composite lifetime of the microwave-treated samples all increase, which is consistent with previous observations. Figure 3e shows the extracted peak position of the GSB signal as a function of time. It is more clearly demonstrated that the microwave treated samples have larger blue-shift distances and longer lifetimes. A larger blue shift indicates a larger hot carrier buildup, and a smaller red shift indicates weaker energy band reorganization, reflecting the stability of the energy bands.

Table 1. Ultrafast Kinetic Process Fitting Parameters

sample			
as-grown	4.42	63.28	784.98
as-grown 30 min UV light irradiation	2.88	61.42	584.98
MW-5s	7.13	190.68	2352.18
MW-5s 30 min UV light irradiation	5.67	181.90	2598.70

To investigate the stability of low-dimensional $CsPbBr_3$ samples after microwave treatment, the PL spectra of the as-grown and the microwave-treated sample after 330 min of UV irradiation are shown in Figure 4a,b, respectively. Compared with the stable peak position of the microwave-treated sample, the emission of the as-grown sample is redshifted from 460 to 525 nm. Figure 4c,d shows the CIE 1931 spatial chromaticity diagrams of the samples in the (x, y) coordinate system, which demonstrate the good color stability of the treated samples. Figure 4e shows the schematic structure of the as-grown and microwave treated samples before and after light irradiation. The results show that the microwave treated sample was able to maintain the blue emission under prolonged irradiation, which indicates the result of stable binding of the ligand to Br^-.

https://doi.org/10.1021/acs.jpcc.3c05919
J. Phys. Chem. C 2023, 127, 23917−23925

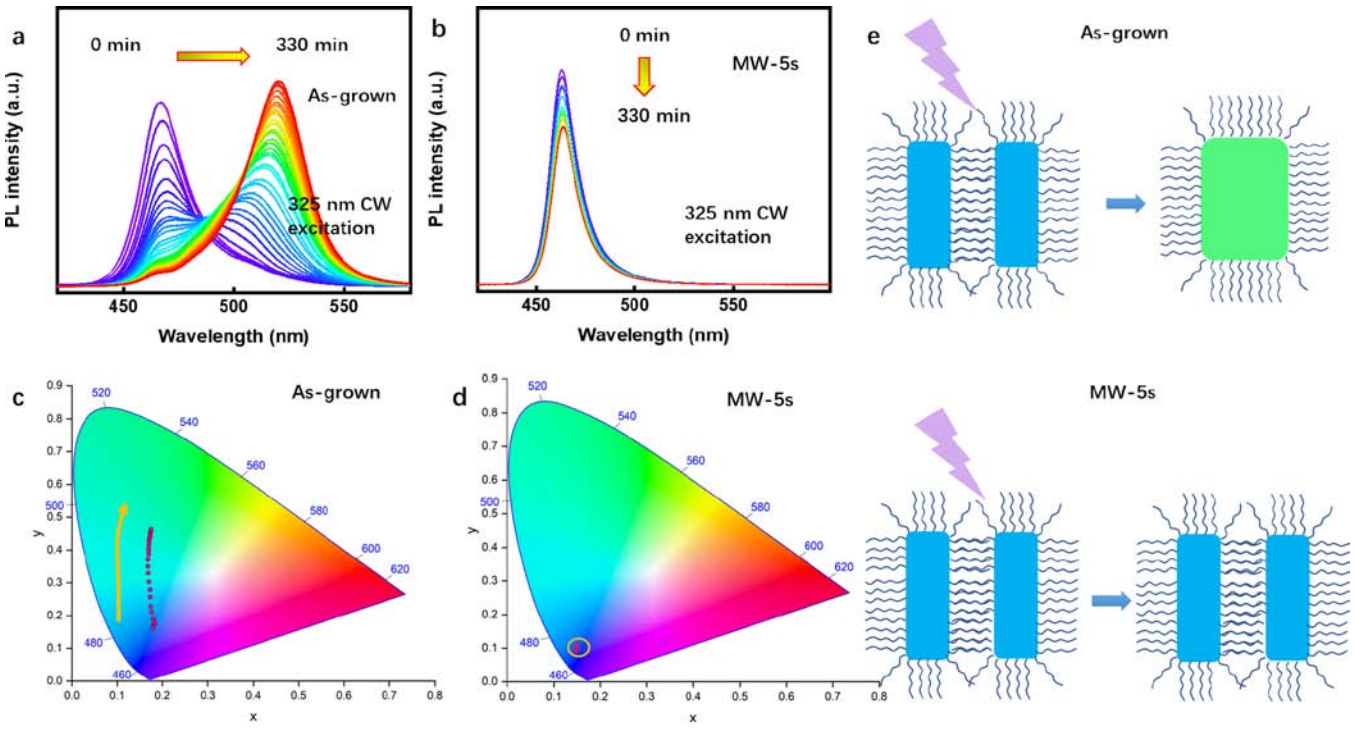

Figure 4. Optical characterization of the change of the sample light irradiation time before and after microwave. (a, b) PL plots of the change in light time of the samples before and after microwave. (c, d) CIE 1931 spatial chromaticity diagrams of the samples in the (x, y) coordinate system. (e) Schematic diagram of the ligand and Br^- structure of the sample before and after microwaving.

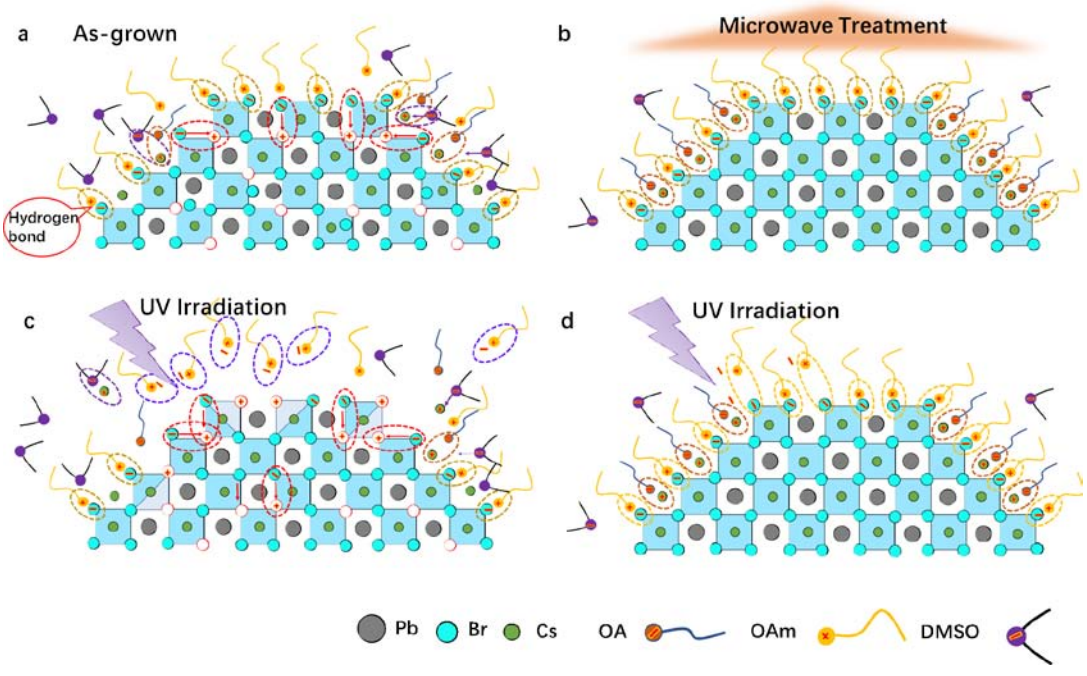

Figure 5. Physical fundamentals of samples before and after microwave and light irradiation. (a, c) Effect of ligand OAm^+, residual polar solution DMSO under as-grown vs UV irradiation conditions. (b, d) Effect of ligand OAm^+, residual polar solution DMSO under microwave conditions vs postmicrowave UV irradiation conditions.

To investigate the physical fundamentals of samples before and after microwave with light irradiation as well as the effect of the ligand and its residual polar solvent DMSO on the low-dimensional $CsPbBr_3$, schematic diagrams of the samples are drawn as shown in Figure 5a,d for samples under the influence of residual polar solvent (DMSO) and UV light irradiation. Among them, OAm^+ and Br^- are bonded by weak hydrogen bonding. In the case of more Br vacancies in the material, the Br on the surface is easily free in the structure due to the Coulombic attraction between the charges. The surface ligand tends to deprotonate by obtaining electrons from the environment, especially for the case under UV irradiation.

https://doi.org/10.1021/acs.jpcc.3c05919
J. Phys. Chem. C 2023, 127, 23917−23925

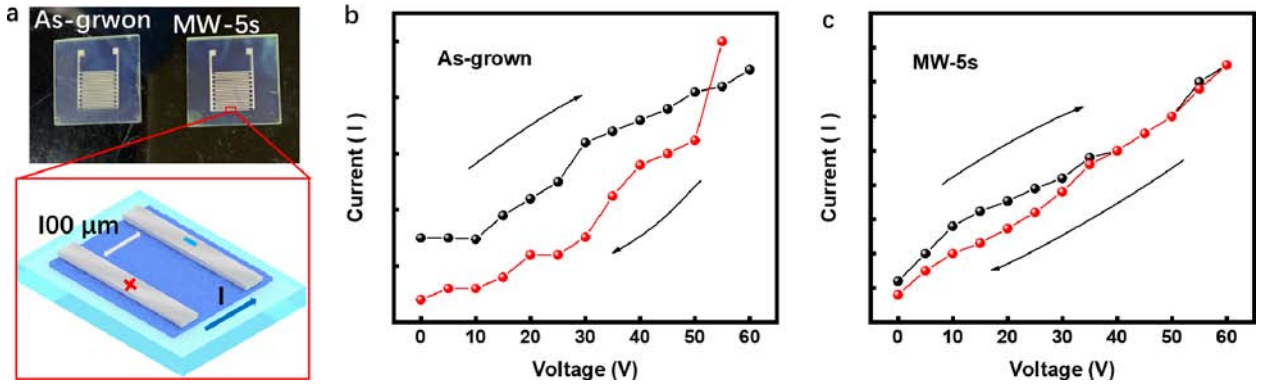

Figure 6. Photoelectric properties of samples. (a) Schematic diagram of the structure of the sample incorporation electrode before and after microwave treatment. (b, c) Voltametric characterization of samples before and after microwave treatment.

Under the dual forces, OAm^+ and Br^- are separated and the ligand becomes free.[28,45,46] In turn, the residual DMSO tends to attract Cs^+ and perovskite tends to decompose, especially under UV irradiation. After microwave treatment, the polar solvent DMSO absorbs microwaves much more than the ligands and perovskite, and the temperature can be eliminated instantaneously above 189 degrees (its vaporization point). Although the microwave absorption of perovskite is smaller than DMSO, the absorbed microwave energy can be effectively transformed to the thermal energy of ions, which can diffuse and fill the vacancy defects. Microwave treatment is particularly effective for perovskite because of its structural peculiarities, which is an ionic compound whose defects are crucial for their structural stability and property. Moreover, the interstitial defects and vacancy defects after microwave annealing are filled and modified, and the internal structure is repaired instantly. This greatly reduces the movement of surface Br^- and indirectly increases the binding of Br^- to the ligand while reducing the ion migration pathway.

This experiment also verified the effect of the microwave treatment on its optoelectronic properties. Figure 6a shows the photoresistor structure of the samples before and after microwave. Figure 6b,c shows the voltametric characteristic (IV) curves of the samples before and after microwave treatment, After the device was energized, the ion migration phenomenon of the samples after MW-5s was significantly reduced compared with that of the as-grown samples, which is very favorable for the optoelectronic devices and provides an effective strategy for the subsequent preparation of stable optoelectronic devices.

CONCLUSIONS

In this work, low-dimensional blue-emitting $CsPbBr_3$ NPLs were prepared, and microwave treatment was performed, which results in samples with better photostability and electrical stability. It is revealed that the conversion of blue-emitting $CsPbBr_3$ to green-emitting $CsPbBr_3$ is due to ligand loss and ion migration. An in-depth analysis of the decay pathway of perovskite using ultrafast kinetics reveals that ligand loss is a deprotonation process (OH^- and H^+ in ambient water and positive and negative charges from light irradiation and power supply), and ion migration is a vacancy-driven and charge redistribution process. After microwave treatment, the residual polar DMSO solvent volatilizes, reducing the chance of structural collapse, and the internal structural defects are reduced (vacancy defects are reduced). In turn, the Br^- ion can exist more stably on its surface, and therefore, it is less likely to lose its hydrogen bond when it binds to external ligands. As a result, the defect migration pathway is reduced, enhancing the ion migration formation energy of the structure. In this process, the hot carriers cooling time becomes longer, and the energy band recombination chances are reduced, which reduces the conversion of hot carriers to nonradiative composite. This study provides a reference for the understanding of the perovskite decay pathway, which will be useful for optimizing and stabilizing blue-emitting optoelectronic devices based on perovskites.

AUTHOR INFORMATION

Corresponding Authors

Ruxue Li − *School of Electronic Engineering and School of Automation, Guangxi University of Science and Technology, Liuzhou, Guangxi 545616, P.R. China*; Email: liruxueic@163.com

Rui Chen − *Department of Electrical and Electronic Engineering, Southern University of Science and Technology, Shenzhen, Guangdong 518055, P.R. China*; orcid.org/0000-0002-0445-7847; Email: chenr@sustech.edu.cn

Authors

Yuanxun Liu − *School of Electronic Engineering and School of Automation, Guangxi University of Science and Technology, Liuzhou, Guangxi 545616, P.R. China*

Ziyuan Xie − *School of Electronic Engineering, Guangxi University of Science and Technology, Liuzhou, Guangxi 545616, P.R. China*

Xuanyu Zhang − *Department of Electrical and Electronic Engineering, Southern University of Science and Technology, Shenzhen, Guangdong 518055, P.R. China*

Huafeng Shi − *Department of Electrical and Electronic Engineering, Southern University of Science and Technology, Shenzhen, Guangdong 518055, P.R. China*

Complete contact information is available at: https://pubs.acs.org/10.1021/acs.jpcc.3c05919

Author Contributions

The manuscript was written through contributions of all authors. All authors have given approval to the final version of the manuscript.

Notes

The authors declare no competing financial interest.

https://doi.org/10.1021/acs.jpcc.3c05919
J. Phys. Chem. C 2023, 127, 23917−23925

■ ACKNOWLEDGMENTS

The authors acknowledge the assistance of SUSTech Core Research Facilities. This is a project supported by the National Natural Science Foundation of China (nos. 11904044 and 62104052), Natural Science Foundation of Guangxi Province (no. 2021GXNSFBA196088), Scientific Research Foundation of Guangxi Education Department (no. 2021KY0345), Scientific Research Starting Foundation of Guangxi University of Science and Technology (no. 21Z03), and Guangxi Colleges and Universities Key Laboratory of Microwave Communication and Micro−Nano Photoelectric Technology.

■ REFERENCES

(1) Cao, Y.; Wang, N.; Tian, H.; Guo, J.; Wei, Y.; Chen, H.; Miao, Y.; Zou, W.; Pan, K.; He, Y.; et al. Perovskite Light-Emitting Diodes Based on Spontaneously Formed Submicrometre-Scale Structures. *Nature* **2018**, *562*, 249−253.

(2) Bati, A. S.; Zhong, Y. L.; Burn, P. L.; Nazeeruddin, M. K.; Shaw, P. E.; Batmunkh, M. Next-Generation Applications for Integrated Perovskite Solar Cells. *Commun Mater.* **2023**, *4*, 2.

(3) Fiuza-Maneiro, N.; Sun, K.; López-Fernández, I.; Gómez-Graña, S.; Müller-Buschbaum, P.; Polavarapu, L. Ligand Chemistry of Inorganic Lead Halide Perovskite Nanocrystals. *ACS Energy Lett.* **2023**, *8*, 1152−1191.

(4) Fakharuddin, A.; Gangishetty, M. K.; Abdi-Jalebi, M.; Chin, S.-H.; bin Mohd Yusoff, A. R.; Congreve, D. N.; Tress, W.; Deschler, F.; Vasilopoulou, M.; Bolink, H. J.; et al. Perovskite Light-Emitting Diodes. *Nat Electron.* **2022**, *5*, 203−216.

(5) Zhang, D.; Chao, L.; Jin, G.; Xing, Z.; Hong, W.; Chen, Y.; Wang, L.; Chen, J.; Ma, D. Highly Efficient Red Perovskite Light-Emitting Diodes with Reduced Efficiency Roll-Off Enabled by Manipulating Crystallization of Quasi-2D Perovskites. *Adv. Funct. Mater.* **2022**, *32*, 2205707.

(6) Liu, Y.; Cui, J.; Du, K.; Tian, H.; He, Z.; Zhou, Q.; Yang, Z.; Deng, Y.; Chen, D.; Zuo, X.; et al. Efficient Blue Light-Emitting Diodes Based on Quantum-Confined Bromide Perovskite Nanostructures. *Nature Photon.* **2019**, *13*, 760−764.

(7) Xing, J.; Zhao, Y.; Askerka, M.; Quan, L. N.; Gong, X.; Zhao, W.; Zhao, J.; Tan, H.; Long, G.; Gao, L.; et al. Color-Stable Highly Luminescent Sky-Blue Perovskite Light-Emitting Diodes. *Nat Commun.* **2018**, *9*, 3541.

(8) Nakamura, S.; Mukai, T.; Senoh, M. Candela-Class High-Brightness Ingan/Algan Double-Heterostructure Blue-Light-Emitting Diodes. *Appl. Phys. Lett.* **1994**, *64*, 1687−1689.

(9) Pacchioni, G. Highly Efficient Perovskite LEDs. *Nat. Rev. Mater.* **2021**, *6*, 108−108.

(10) Zhang, Q.; Zhang, D.; Fu, Y.; Poddar, S.; Shu, L.; Mo, X.; Fan, Z. Light out-Coupling Management in Perovskite LEDs—What Can We Learn from the Past? *Adv. Funct. Mater.* **2020**, *30*, 2002570.

(11) Zhang, J.; Zhang, T.; Ma, Z.; Yuan, F.; Zhou, X.; Wang, H.; Liu, Z.; Qing, J.; Chen, H.; Li, X.; Su, S.; Xie, J.; Shi, Z.; Hou, L.; Shan, C. A Multifunctional "Halide-Equivalent" Anion Enabling Efficient Cspb $(Br/I)_3$ Nanocrystals Pure-Red Light-Emitting Diodes with External Quantum Efficiency Exceeding 23%. *Adv. Mater.* **2023**, *35*, 2209002.

(12) Sun, Y.; Ge, L.; Dai, L.; Cho, C.; Ferrer Orri, J.; Ji, K.; Zelewski, S. J.; Liu, Y.; Mirabelli, A. J.; Zhang, Y.; et al. Bright and Stable Perovskite Light-Emitting Diodes in the near-Infrared Range. *Nature* **2023**, *615*, 830−835.

(13) Peng, S.; Wang, S.; Zhao, D.; Li, X.; Liang, C.; Xia, J.; Zhang, T.; Xing, G.; Tang, Z. Pure Bromide-Based Perovskite Nanoplatelets for Blue Light-Emitting Diodes. *Small Methods* **2019**, *3*, 1900196.

(14) Ge, C.; Fang, Q.; Lin, H.; Hu, H. Review on Blue Perovskite Light-Emitting Diodes: Recent Advances and Future Prospects. *Front. Mater.* **2021**, *8*, No. 635025.

(15) Li, Z.; Cao, K.; Li, J.; Tang, Y.; Ding, X.; Yu, B. Review of Blue Perovskite Light Emitting Diodes with Optimization Strategies for Perovskite Film and Device Structure. *Opto-Electron. Adv.* **2021**, *4*, 20001901.

(16) Wang, H.; Zhao, X.; Zhang, B.; Xie, Z. Blue Perovskite Light-Emitting Diodes Based on Rbx-Doped Polycrystalline $CsPbBr_3$ Perovskite Films. *J. Mater. Chem. C.* **2019**, *7*, 5596−5603.

(17) Rybin, N.; Ghosh, D.; Tisdale, J.; Shrestha, S.; Yoho, M.; Vo, D.; Even, J.; Katan, C.; Nie, W.; Neukirch, A. J.; Tretiak, S. Effects of Chlorine Mixing on Optoelectronics, Ion Migration, and Gamma-Ray Detection in Bromide Perovskites. *Chem. Mater.* **2020**, *32*, 1854−1863.

(18) Li, Z.; Zheng, X.; Xiao, X.; An, Y.; Wang, Y.; Huang, Q.; Li, X.; Cheacharoen, R.; An, Q.; Rong, Y.; et al. Beyond the Phase Segregation: Probing the Irreversible Phase Reconstruction of Mixed-Halide Perovskites. *Adv. Sci.* **2022**, *9*, 2103948.

(19) Bischak, C. G.; Hetherington, C. L.; Wu, H.; Aloni, S.; Ogletree, D. F.; Limmer, D. T.; Ginsberg, N. S. Origin of Reversible Photoinduced Phase Separation in Hybrid Perovskites. *Nano Lett.* **2017**, *17*, 1028−1033.

(20) Chen, Y. C.; Chou, H. L.; Lin, J. C.; Lee, Y. C.; Pao, C. W.; Chen, J. L.; Chang, C. C.; Chi, R. Y.; Kuo, T. R.; Lu, C. W.; Wang, D. Y. Enhanced Luminescence and Stability of Cesium Lead Halide Perovskite $CsPbX_3$ Nanocrystals by Cu^{2+}-Assisted Anion Exchange Reactions. *J. Phys. Chem. C* **2019**, *123*, 2353−2360.

(21) Chiba, T.; Ishikawa, S.; Sato, J.; Takahashi, Y.; Ebe, H.; Ohisa, S.; Kido, J. Blue Perovskite Nanocrystal Light-Emitting Devices Via the Ligand Exchange with Adamantane Diamine. *Adv. Opt. Mater.* **2020**, *8*, 2000289.

(22) Bi, C.; Yao, Z.; Sun, X.; Wei, X.; Wang, J.; Tian, J. Perovskite Quantum Dots with Ultralow Trap Density by Acid Etching-Driven Ligand Exchange for High Luminance and Stable Pure-Blue Light-Emitting Diodes. *Adv. Mater.* **2021**, *33*, 2006722.

(23) Wu, Y.; Wei, C.; Li, X.; Li, Y.; Qiu, S.; Shen, W.; Cai, B.; Sun, Z.; Yang, D.; Deng, Z.; et al. In Situ Passivation of $PbBr_6^{4-}$ Octahedra toward Blue Luminescent $CsPbBr_3$ Nanoplatelets with near 100% Absolute Quantum Yield. *ACS Energy Lett.* **2018**, *3*, 2030−2037.

(24) DuBose, J. T.; Kamat, P. V. Surface Chemistry Matters. How Ligands Influence Excited State Interactions between $CsPbBr_3$ and Methyl Viologen. *J. Phys. Chem. C.* **2020**, *124*, 12990−12998.

(25) Zhou, F.; Li, Z.; Chen, H.; Wang, Q.; Ding, L.; Jin, Z. Application of Perovskite Nanocrystals (NCs)/Quantum Dots (QDs) in Solar Cells. *Nano Energy.* **2020**, *73*, No. 104757.

(26) Bai, Y.; Hao, M.; Ding, S.; Chen, P.; Wang, L. Surface Chemistry Engineering of Perovskite Quantum Dots: Strategies, Applications, and Perspectives. *Adv. Mater.* **2022**, *34*, 2105958.

(27) Sun, Y.; Zhang, H.; Zhu, K.; Ye, W.; She, L.; Gao, X.; Ji, W.; Zeng, Q. Research on the Influence of Polar Solvents on $CsPbPr_3$ Perovskite QDs. *RSC Adv.* **2021**, *11*, 27333−27337.

(28) Holekevi Chandrappa, M. L.; Zhu, Z.; Fenning, D. P.; Ong, S. P. Correlated Octahedral Rotation and Organic Cation Reorientation Assist Halide Ion Migration in Lead Halide Perovskites. *Chem. Mater.* **2021**, *33*, 4672−4678.

(29) Bischak, C. G.; Wong, A. B.; Lin, E.; Limmer, D. T.; Yang, P.; Ginsberg, N. S. Tunable Polaron Distortions Control the Extent of Halide Demixing in Lead Halide Perovskites. *J. Phys. Chem. Lett.* **2018**, *9*, 3998−4005.

(30) Zou, Y.; Xu, H.; Li, S.; Song, T.; Kuai, L.; Bai, S.; Gao, F.; Sun, B. Spectral-Stable Blue Emission from Moisture-Treated Low-Dimensional Lead Bromide-Based Perovskite Films. *ACS Photonics.* **2019**, *6*, 1728−1735.

(31) More, S. A.; Halor, R. G.; Shaikh, R.; Bisen, G. G.; Tarkas, H. S.; Tak, S. R.; Bade, B. R.; Jadkar, S. R.; Sali, J. V.; Ghosh, S. S.; et al. Investigating the Effect of Solvent Vapours on Crystallinity, Phase, and Optical, Morphological and Structural Properties of Organ lead Halide Perovskite Films. *RSC Adv.* **2020**, *10*, 39995−40004.

(32) Cao, J.; Yan, C.; Luo, C.; Li, W.; Zeng, X.; Xu, Z.; Fu, X.; Wang, Q.; Chu, X.; Huang, H.; et al. Cryogenic-Temperature Thermodynamically Suppressed and Strongly Confined $CsPbBr_3$ Quantum Dots for Deeply Blue Light-Emitting Diodes. *Adv. Opt. Mater.* **2021**, *9*, 2100300.

(33) Li, R.; Li, B.; Fang, X.; Wang, D.; Shi, Y.; Liu, X.; Chen, R.; Wei, Z. Self-Structural Healing of Encapsulated Perovskite Microcrystals for Improved Optical and Thermal Stability. *Adv. Mater.* **2021**, *33*, 2100466.
(34) Wang, H.; Dong, Z.; Liu, H.; Li, W.; Zhu, L.; Chen, H. Roles of Organic Molecules in Inorganic $CsPbX_3$ Perovskite Solar Cells. *Adv. Energy Mater.* **2021**, *11*, 2002940.
(35) Liu, H.; Worku, M.; Mondal, A.; Shonde, T. B.; Chaaban, M.; Ben-Akacha, A.; Lee, S.; Gonzalez, F.; Olasupo, O.; Lin, X.; et al. Efficient and Stable Blue Light Emitting Diodes Based on $CsPbBr_3$ Nanoplatelets with Surface Passivation by a Multifunctional Organic Sulfate. *Adv. Energy Mater.* **2023**, *13*, 2201605.
(36) Li, R.; Yu, J.; Wang, S.; Shi, Y.; Wang, Z.; Wang, K.; Ni, Z.; Yang, X.; Wei, Z.; Chen, R.; et al. Surface Modification of All-Inorganic Halide Perovskite Nanorods by a Microscale Hydrophobic Zeolite for Stable and Sensitive Laser Humidity Sensing. *Nanoscale* **2020**, *12*, 13360−13367.
(37) Qian, X.-Y.; Tang, Y.-Y.; Zhou, W.; Shen, Y.; Guo, M.-L.; Li, Y. Q.; Tang, J.-X. Strategies to Improve Luminescence Efficiency and Stability of Blue Perovskite Light-Emitting Devices. *Small Science* **2021**, *1*, 2000048.
(38) Chen, Q.; Ma, T.; Wang, F.; Liu, Y.; Liu, S.; Wang, J.; Cheng, Z.; Chang, Q.; Yang, R.; Huang, W.; et al. Rapid Microwave-Annealing Process of Hybrid Perovskites to Eliminate Miscellaneous Phase for High Performance Photovoltaics. *Adv. Sci.* **2020**, *7*, 2000480.
(39) Zhou, W.; Liu, S.; Chen, W.; Li, H.; Yan, S.; Yu, J.; Liu, C.; Zhao, L.; Zeng, T.; Han, T.; et al. Efficient and Self-Healing Copper Halide $Cs_3Cu_2Cl_5$ Film Assisted by Microwave Treatment for High-Resolution X-ray Imaging. *Ceram. Int.* **2022**, *48*, 25086−25093.
(40) Barua, P.; In, C. M.; Lee, M. J.; Hwang, I. Microwave-Facilitated Crystal Growth of Defect-Passivated Triple-Cation Metal Halide Perovskites toward Efficient Solar Cells. *Nanoscale* **2023**, *15*, 5954−5963.
(41) Zhang, X.; Pang, G.; Xing, G.; Chen, R. Temperature Dependent Optical Characteristics of All-Inorganic $CsPbBr_3$ Nanocrystals Film. *Mater. Today Phys.* **2020**, *15*, No. 100259.
(42) Wei, Q.; Yin, J.; Bakr, O. M.; Wang, Z.; Wang, C.; Mohammed, O. F.; Li, M.; Xing, G. Effect of Zinc-Doping on the Reduction of the Hot-Carrier Cooling Rate in Halide Perovskites. *Angew. Chem., Int. Ed.* **2021**, *60*, 10957−10963.
(43) Zeng, P.; Ren, X.; Wei, L.; Zhao, H.; Liu, X.; Zhang, X.; Xu, Y.; Yan, L.; Boldt, K.; Smith, T. A.; Liu, M. Control of Hot Carrier Relaxation in $CsPbBr_3$ Nanocrystals Using Damping Ligands. *Angew. Chem.* **2022**, *134*, No. e202111443.
(44) Doherty, T. A.; Winchester, A. J.; Macpherson, S.; Johnstone, D. N.; Pareek, V.; Tennyson, E. M.; Kosar, S.; Kosasih, F. U.; Anaya, M.; Abdi-Jalebi, M.; et al. Performance-limiting nanoscale trap clusters at grain junctions in halide perovskites. *Nature* **2020**, *580*, 360−366.
(45) Guo, Y.; Yin, X.; Liu, D.; Liu, J.; Zhang, C.; Xie, H.; Yang, Y.; Que, W. Photoinduced Self-Healing of Halide Segregation in Mixed-Halide Perovskites. *ACS Energy Lett.* **2021**, *6*, 2502−2511.
(46) Vale, B. R. C.; Socie, E.; Burgos-Caminal, A.; Bettini, J.; Schiavon, M. A.; Moser, J. E. Exciton, Biexciton, and Hot Exciton Dynamics in $CsPbBr_3$ Colloidal Nanoplatelets. *J. Phys. Chem. Lett.* **2019**, *11*, 387−394.

https://doi.org/10.1021/acs.jpcc.3c05919
J. Phys. Chem. C 2023, 127, 23917−23925